

Direct numerical simulation of hypersonic turbulent boundary layers. Part 3. Effect of Mach number

L. DUAN, I. BEEKMAN AND M. P. MARTÍN†

Department of Aerospace Engineering, University of Maryland, College Park, MD 20742, USA

(Received 18 February 2010; revised 20 October 2010; accepted 11 November 2010;
first published online 2 March 2011)

In this paper, we perform direct numerical simulations (DNS) of turbulent boundary layers with nominal free-stream Mach number ranging from 0.3 to 12. The main objective is to assess the scalings with respect to the mean and turbulence behaviours as well as the possible breakdown of the weak compressibility hypothesis for turbulent boundary layers at high Mach numbers ($M > 5$). We find that many of the scaling relations, such as the van Driest transformation for mean velocity, Walz's relation, Morkovin's scaling and the strong Reynolds analogy, which are derived based on the weak compressibility hypothesis, remain valid for the range of free-stream Mach numbers considered. The explicit dilatation terms such as pressure dilatation and dilatational dissipation remain small for the present Mach number range, and the pressure–strain correlation and the anisotropy of the Reynolds stress tensor are insensitive to the free-stream Mach number. The possible effects of intrinsic compressibility are reflected by the increase in the fluctuations of thermodynamic quantities (p'_{rms}/p_w , $\rho'_{rms}/\bar{\rho}$, T'_{rms}/\bar{T}) and turbulence Mach numbers (M_t , M'_{rms}), the existence of shocklets, the modification of turbulence structures (near-wall streaks and large-scale motions) and the variation in the onset of intermittency.

Key words: compressible turbulence, high-speed flow, turbulent boundary layers

1. Introduction

An essential part of the study of compressible turbulent boundary layers is to check the validity of Morkovin's hypothesis. The hypothesis, first proposed by Morkovin (1962), is that, at moderate free-stream Mach numbers ($M \leq 5$), dilatation is small and any differences from incompressible turbulence can be accounted for by mean variations of fluid properties. This is the basis of the van Driest transformation, a velocity scaling that accounts for the fluid-property variations to collapse compressible flow data onto the 'universal' incompressible distribution. The check for validity of Morkovin's hypothesis consists primarily of experiments and numerical simulations at moderate Mach numbers (Fernholz & Finley 1980; Guarini *et al.* 2000; Pirozzoli, Grasso & Gatski 2004). Both experiments and numerical simulations confirmed that at moderate Mach numbers, the essential dynamics of the investigated supersonic turbulent boundary layers closely resemble the incompressible pattern under analogous conditions.

† Email address for correspondence: pmartin@umiacs.umd.edu

There are only limited studies of boundary layers at high Mach numbers. For example, one particularly important experiment was performed at Mach 6.7 at NASA Ames (Owen & Horstman 1972*a,b*; Owen, Horstman & Kussoy 1975; Mikulla & Horstman 1976). Similar measurements were done at Mach 7.2 by Baumgartner (1997), at Mach 11 by McGinley, Spina & Sheplak (1994), and more recently at Mach 7.2 by Sahoo, Schultze & Smits (2009). In terms of numerical simulations, Martín (2004) performed direct numerical simulations (DNS) with free-stream Mach numbers varying from 3 to 8. Maeder, Adams & Kleiser (2001) conducted DNS at Mach numbers 3, 4.5 and 6. Both previous experimental measurements and numerical simulations at high Mach numbers have shown that the mean profile followed the standard semi-logarithmic profile when van Driest transformation is applied. Together these data support the notion that the scaling laws for the mean flow are essentially independent of Mach numbers.

However, the scaling with respect to turbulence behaviour is still not so clear. Experimentally, two of the very few datasets on hypersonic turbulence measurements using hot-wire anemometry, by Owen *et al.* (1975) and McGinley *et al.* (1994), showed that the turbulence intensities were significantly smaller than seen in incompressible flows and do not scale according to Morkovin. However, the data from the more recent and preliminary experiment by Sahoo *et al.* (2009) for a flat-plate boundary layer at Mach 7.2 using particle image velocimetry (PIV) gave much larger turbulence intensities than the measurement by Owen *et al.* (1975) and scale better according to Morkovin. Intrinsic difficulties exist in both measurements by hot-wire anemometry and PIV. The hot-wire data might have suffered from poor frequency response and/or suspect calibrations of the hot-wire anemometry used in the measurements, as observed by McGinley *et al.* (1994), and the PIV measurement might also suffer from low seeding density in the context of strong gradients. In addition, the reported turbulence statistics might be influenced by the spatial resolution of the measurements, namely the size of the hot wire or the interrogation volume for PIV.

Numerically, the DNS by Maeder *et al.* (2001) showed that the compressible profiles of Reynolds stresses have a shape similar to the incompressible profiles, though they are fuller in the wake region for higher Mach numbers. However, as they mentioned, it remains to be assessed whether this is an artefact of their simulation caused by the relatively short domain. So far, nearly all the comparisons of turbulence quantities between numerical solutions and experiments for compressible boundary layers are achieved only at moderate Mach numbers, and there are still no direct comparisons between numerics and experiments for boundary layers with free-stream Mach number above 5.

One purpose of the current study is to achieve direct comparison of numerical results with the recent experimental data at Mach 7.2 by Sahoo *et al.* (2009), and further investigate turbulence scalings with a wide range of free-stream Mach numbers using DNS, which provides more detailed turbulence statistics than experiments.

Besides turbulence statistics, another purpose of the current study is to investigate the effects of free-stream Mach number on coherent turbulence structures, since recent laboratory and numerical experiments indicate that these structures play a key role in wall-bounded turbulent flows at incompressible and compressible conditions (Robinson 1991; Spina, Smits & Robinson 1994; Kim & Adrian 1999; Adrian, Meinhart & Tomkins 2000; Ganapathisubramani, Clemens & Dolling 2006; Hutchins & Marusic 2007; Ringuette, Wu & Martín 2008).

This paper is structured as follows. Flow conditions and simulation details are given in §2. Turbulence statistics are given in §3. The strong Reynolds analogy and

Case	M_δ	ρ_δ (kg m ⁻³)	T_δ (K)	T_w/T_δ	Re_θ	Re_τ	Re_{δ_2}	θ (mm)	H	δ (mm)
M0	0.30	0.0900	220.0	1.00	1514.7.6	569.9	1515.2	2.76	1.41	23.0
M3	2.97	0.0910	219.9	2.51	3028.6	486.9	1586.7	0.619	5.09	8.85
M4	3.98	0.0902	219.2	3.83	4093.7	438.2	1587.4	0.658	8.01	12.0
M5	4.90	0.0962	224.4	5.31	4931.7	416.5	1578.0	0.682	11.29	15.1
M6	5.81	0.0990	230.7	7.02	5775.1	412.8	1582.2	0.730	15.4	19.7
M7	6.89	0.0929	224.2	9.49	7207.3	391.7	1586.4	0.838	20.2	28.1
M8	7.70	0.0990	232.8	11.2	7508.3	397.5	1577.5	0.861	24.2	31.8
M12	11.93	0.0906	228.0	27.6	11356.4	376.8	1577.5	1.33	46.1	84.7

TABLE 1. Dimensional boundary-layer edge and wall parameters for the DNS database.

the turbulent kinetic energy budget are given in §§4 and 5, respectively. The effect of compressibility is investigated in §6. Turbulence structure analysis is given in §7. Finally, conclusions are drawn in §8.

2. Simulation details

2.1. Flow conditions

To study Mach number effects, we use a DNS database of turbulent boundary layers (Martín 2004, 2007) with nominal free-stream Mach numbers ranging from 3 to 12, with an additional incompressible reference case. The boundary-layer edge conditions and wall parameters for the DNS database are given in table 1, which provides boundary-layer edge Mach number, density and temperature, M_δ , ρ_δ and T_δ , respectively, and boundary-layer properties, namely momentum thickness θ , shape factor $H = \delta^*/\theta$, with δ^* being the displacement thickness, boundary-layer thickness δ , and different definitions of Reynolds number, where $Re_\theta \equiv \rho_\delta u_\delta \theta / \mu_\delta$, $Re_\tau \equiv \rho_w u_\tau \delta / \mu_w$ and $Re_{\delta_2} \equiv \rho_\delta u_\delta \theta / \mu_w$. We have used subscripts δ and w to denote quantities at the boundary-layer edge and at the wall, respectively. Here u_τ is the friction velocity defined as $u_\tau = \sqrt{\tau_w / \rho_w}$, with τ_w being the wall shear stress. For all cases, the wall condition is isothermal and prescribed to be nearly the adiabatic temperature.

To isolate the effect of varying free-stream Mach number, it is desirable to match the Reynolds number of the different cases. Here, we keep Re_τ and Re_{δ_2} nearly constant, with insignificant variation of Re_θ across the cases.

2.2. Numerical simulation parameters

Following Martín (2007), the computational domain size and grid resolution are determined based on the characteristic large length scale, δ , and the characteristic small, near-wall length scale z_τ , respectively. The computational domain must be large enough to contain a good sample of the large scales, while the grid resolution must be fine enough to resolve the near-wall structures. The domain size ($L_x \times L_y \times L_z$), the grid size ($\Delta x \times \Delta y \times \Delta z$) and the number of grid points ($N_x \times N_y \times N_z$) are given in table 2. We take the streamwise, spanwise and wall-normal directions to be x , y and z , respectively. Uniform grids are used in the streamwise and spanwise directions as Δx^+ and Δy^+ , where the superscript (+) indicates scaling with inner or wall values. Geometrically stretched grids are used in the wall-normal direction, with $z_k = z_2(\alpha^{k-1} - 1)/(\alpha - 1)$. The governing equations, numerical method, boundary conditions and initialization procedure are given in Martín (2007). The working fluid is calorically perfect air.

Case	L_x/δ	L_y/δ	L_z/δ	Δx^+	Δy^+	z_2^+	α	N_x	N_y	N_z
M0	8.3	2.4	4.0	7.9	3.4	0.10	1.070	600	400	110
M3	8.7	2.7	7.8	8.4	3.4	0.30	1.063	512	384	110
M4	8.8	2.5	8.8	7.5	2.9	0.29	1.064	512	384	110
M5	9.9	2.6	8.8	6.9	2.7	0.25	1.065	600	400	110
M6	9.7	2.9	9.7	7.8	3.1	0.30	1.064	512	384	110
M7	8.7	2.5	8.7	6.7	2.6	0.27	1.063	512	384	110
M8	9.4	2.6	9.3	7.3	2.7	0.30	1.063	512	384	110
M12	10.9	2.4	15.9	6.8	2.3	0.27	1.063	600	400	120

TABLE 2. Grid resolution and domain size for the DNS.

In the results that follow, both Reynolds and Favre averaging are used depending on the simplicity of presentation and conventions used in the papers to which we are comparing. The Reynolds average of f over the x - and y -directions will be denoted by \bar{f} or $\langle f \rangle$, and fluctuations about this mean will be denoted by f' . The Favre average over the x - and y -directions, \tilde{f} , is a density-weighted average:

$$\tilde{f} = \frac{\overline{\rho f}}{\bar{\rho}}. \quad (2.1)$$

Fluctuations about the Favre average will be denoted by f'' .

To assess the adequacy of the domain size, streamwise and spanwise two-point correlations for the streamwise, spanwise and wall-normal velocity components as well as for density and temperature are plotted. Figure 1 shows that the streamwise and spanwise two-point correlations are nearly zero at large separations for both cases M3 and M12. Similar results can be shown for other cases.

The grid resolution can be assessed by conducting grid-convergence studies. Figures 2(a) and 2(b) plot the r.m.s. of streamwise velocity normalized by friction velocity and the r.m.s. of temperature normalized by mean temperature, respectively, for M3 and M12 with different number of grid points. All the corresponding curves collapse to within 1 %, indicating the grid is fine enough to converge the results. Grid convergence has been checked for all the other cases.

Another indication of the adequacy of the resolution is the value of $k_{max}\eta$, where k_{max} is the maximum wavenumber in x and η is the local Kolmogorov scale. The maximum and minimum of this value in current DNS are 1.7 and 0.7, respectively, which is adequate. For comparison, the DNS of a supersonic boundary layer at Mach 2.5 conducted by Guarini *et al.* (2000) had values of 1.6 and 0.5 for the maximum and minimum of $k_{max}\eta$, respectively.

Further assessment of grid resolution near the wall can be conducted by comparing with DNS-calculated skin friction C_f with well-established semi-empirical results. Table 3 gives the DNS-calculated skin friction and the skin friction predicted by van Driest II theory (van Driest 1956). It is shown that DNS-calculated skin frictions are within 5 % of the van Driest II prediction for all cases.

DNS results have been compared with existing experimental data at both moderate and high Mach numbers, including the experimental flow conditions of Debiève (1983), Debiève, Gouin & Gaviglio (1981) and Fernholz *et al.* (1989) at $M = 2.32$ and $Re_\theta = 4450$, and the experimental flow conditions of Sahoo *et al.* (2009) at $M = 7.2$ and $Re_\theta = 3300$. The details of the comparison at the former conditions are given in Martín (2007). Recent developments in PIV measurements allow for detailed velocity surveys

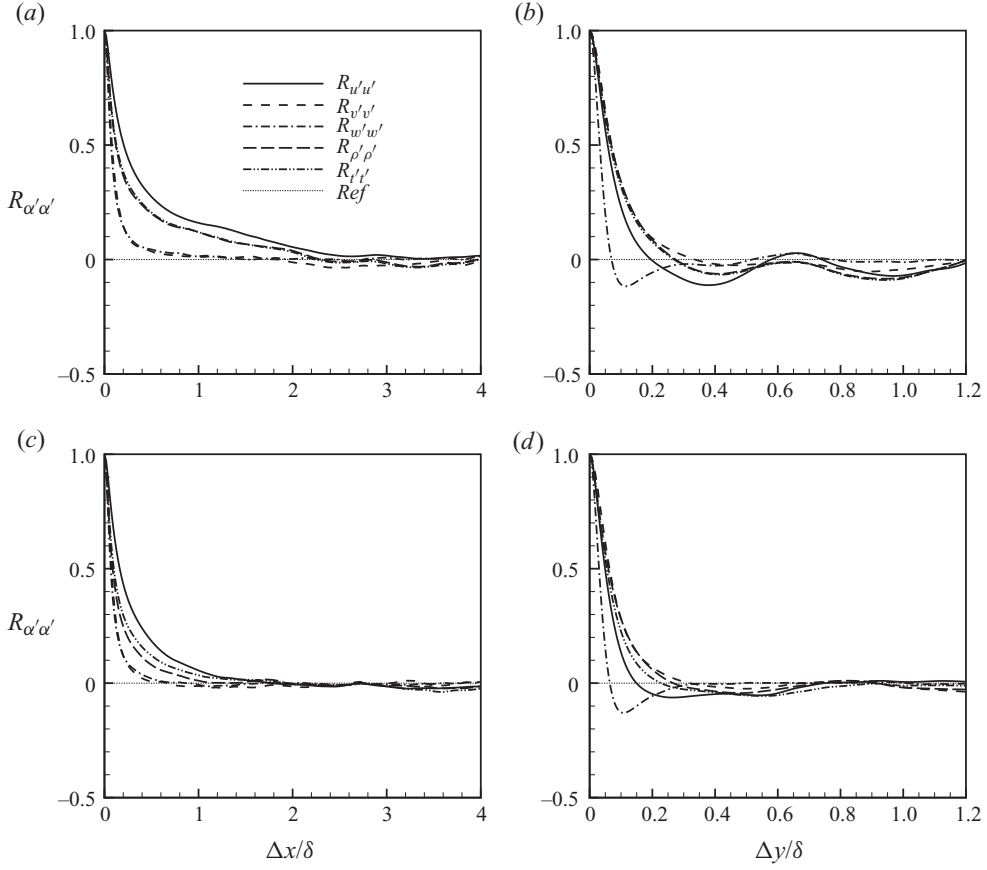


FIGURE 1. Two-point correlations $R_{\alpha'\alpha'}$ for the streamwise, spanwise and wall-normal velocity components, density and temperature at $z/\delta = 0.1$. Plotted versus (a) $\Delta x/\delta$ for M3, (b) $\Delta y/\delta$ for M3, (c) $\Delta x/\delta$ for M12, (d) $\Delta y/\delta$ for M12. The dotted line represents the zero value.

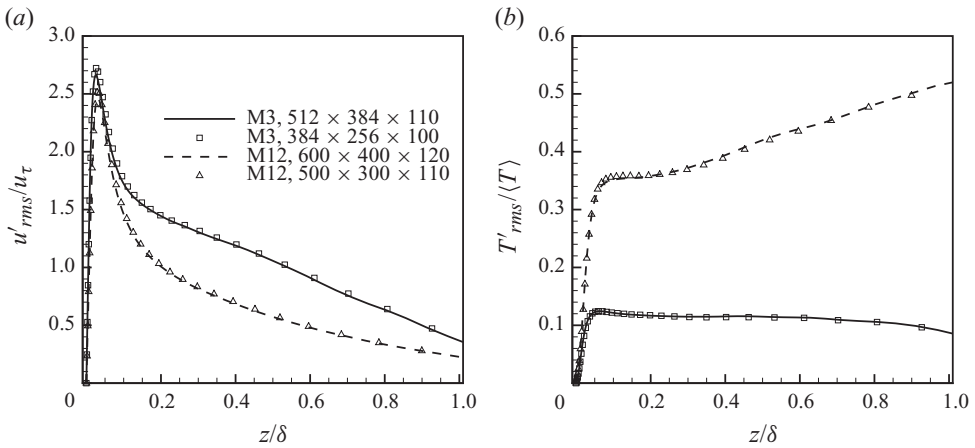


FIGURE 2. Convergence study for M3 and M12 varying grid sizes, $N_x \times N_y \times N_z$.

Case	C_f	$(C_f)_{\text{vanDriestII}}$
M0	4.08×10^{-3}	3.86×10^{-3}
M3	2.17×10^{-3}	2.08×10^{-3}
M4	1.61×10^{-3}	1.55×10^{-3}
M5	1.31×10^{-3}	1.27×10^{-3}
M6	1.08×10^{-3}	1.07×10^{-3}
M7	8.51×10^{-4}	8.47×10^{-4}
M8	7.80×10^{-4}	7.96×10^{-4}
M12	4.60×10^{-4}	5.00×10^{-4}

TABLE 3. Skin friction of DNS database against that predicted by van Driest II theory (van Driest 1956) for different free-stream Mach number cases.

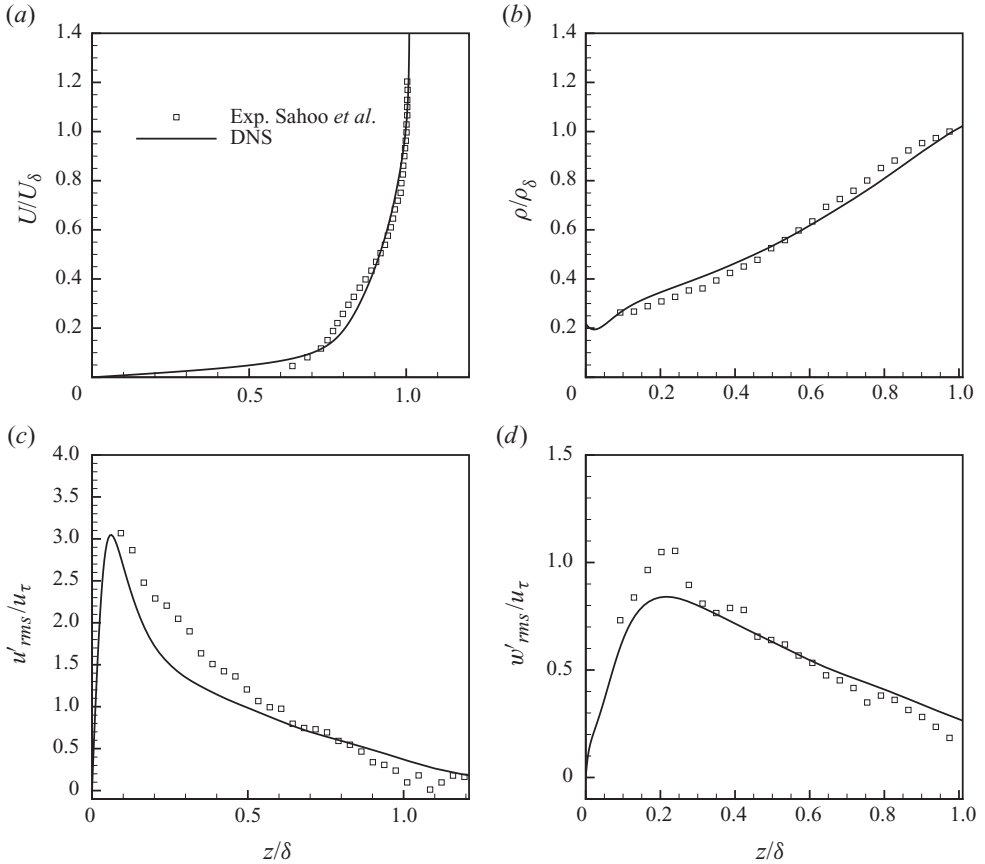


FIGURE 3. (a–d) Comparison between the DNS and the preliminary PIV experiment by Sahoo *et al.* (2009) at $Ma_\delta = 7.2$ and Re_θ approximately 3300.

at high Mach numbers. Figure 3 plots the comparison at $M = 7.2$ and $Re_\theta = 3300$, where the mean velocity and density and the streamwise and wall-normal turbulence intensities are plotted for both the DNS and the preliminary experimental data. It is shown that good agreement is achieved between DNS and the experiment. There are discrepancies in the velocity intensities close to the wall, which is probably due to the inaccuracy in the PIV data. Nevertheless, these are the first of presently developing

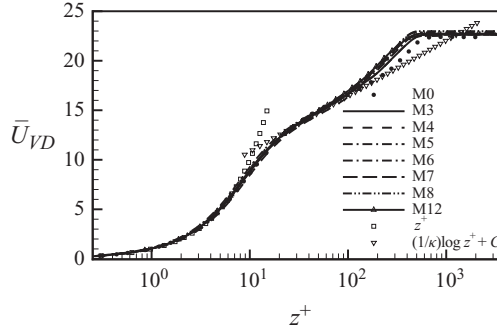


FIGURE 4. Van Driest transformed velocity for different free-stream Mach number cases.

PIV measurements at such a high Mach number, and this is the first direct comparison between a DNS and an experiment at Mach number greater than 5.

3. Turbulence statistics

For all cases, averages are computed over streamwise and spanwise directions of each field; then an ensemble average is calculated over fields spanning over more than $20\delta/u_\delta$, with u_δ being the boundary-layer edge velocity. Using periodic boundary conditions, the change in (δ^*, u_τ, Cf) across the fields for ensemble averaging is less than 5% and the flow can be viewed as a good approximation of a boundary layer at a static station (see Xu & Martín 2004).

3.1. Mean flow

Figure 4 plots the van Driest transformed velocity \bar{U}_{VD} , for different Mach number cases, which is defined as

$$\bar{U}_{VD} = \frac{1}{\bar{u}_\tau} \int_0^U (\bar{T}_w/\bar{T})^{1/2} dU. \quad (3.1)$$

The profiles of \bar{U}_{VD} for various Mach number cases collapse extremely well. The log region can be very well described by $(1/\kappa)\log z^+ + C$, with $\kappa = 0.41$ and $C = 5.2$.

One of the commonly used temperature–velocity relationships for zero-pressure-gradient boundary layers is Walz’s equation or Crocco’s relation (Walz 1969):

$$\frac{\bar{T}}{\bar{T}_\delta} = \frac{\bar{T}_w}{\bar{T}_\delta} + \frac{\bar{T}_r - \bar{T}_w}{\bar{T}_\delta} \left(\frac{\bar{u}}{\bar{u}_\delta} \right) + \frac{\bar{T}_\delta - \bar{T}_r}{\bar{T}_\delta} \left(\frac{\bar{u}}{\bar{u}_\delta} \right)^2. \quad (3.2)$$

Figure 5 shows the comparison between (3.2) and DNS results. It is shown that there is excellent agreement for all the Mach number cases.

3.2. Turbulence quantities

Figure 6(a–f) plots turbulence intensities and density-weighted intensities in streamwise, spanwise and wall-normal directions across boundary layers for different free-stream Mach number cases. It is shown that turbulence intensities decrease with free-stream Mach number for all directions, and a much better collapse of the data is achieved by Morkovin’s scaling, which takes into account the variation in mean

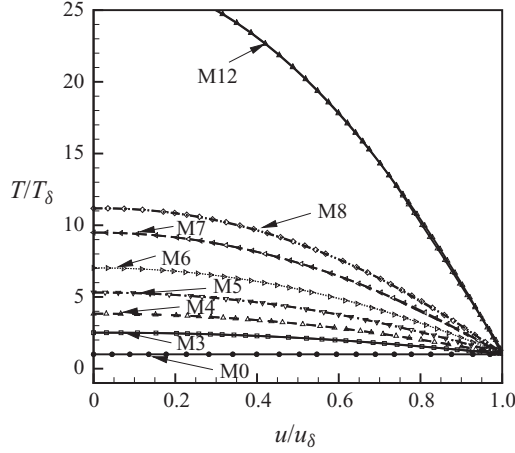


FIGURE 5. Test of Walz's equation, as expressed by (3.2) for cases with different free-stream Mach numbers. Lines, DNS; symbols, Walz's relation given by (3.2).

flow properties. A similar trend is observed for the Reynolds shear stress, as shown in figure 7(a, b).

Figure 8(a, b) plots r.m.s. values of pressure fluctuation normalized by \bar{p}_w and $\bar{\rho}_w u_\tau^2$, respectively. It is shown that the magnitude of pressure fluctuations increases significantly with increasing free-stream Mach number when normalized by \bar{p}_w . A better collapse of the data is achieved when p'_{rms} is normalized by $\bar{\rho}_w u_\tau^2$.

Figure 9(a, b) plots r.m.s. values of density and temperature fluctuations normalized by mean values. Similar to the pressure fluctuation, we observe a dramatic increase in the magnitude of fluctuations when the free-stream Mach number is increased.

4. Reynolds analogies

Morkovin (1962) proposed five strong Reynolds analogy (SRA) relations. Three of them are as follows:

$$\frac{T''_{rms}/\tilde{T}}{(\gamma - 1)M_a^2(u''_{rms}/\tilde{u})} \approx 1, \quad (4.1)$$

$$-R_{u''T''} \approx 1, \quad (4.2)$$

$$Pr_t = \frac{\overline{\rho u'' w''}(\partial \tilde{T}/\partial z)}{\overline{\rho w'' T''}(\partial \tilde{u}/\partial z)} \approx 1. \quad (4.3)$$

Figure 10(a) plots the relationship between r.m.s. temperature and streamwise velocity fluctuations, as expressed by (4.1), for supersonic free-stream Mach number cases. It is shown that the agreement of relation (4.1) is not perfect with all the Mach number cases. Figure 10(b) shows that better agreement is achieved between current DNS results and the modified Reynolds analogy of Huang, Coleman & Bradshaw (1995), which is given by

$$\frac{T''_{rms}/\tilde{T}}{(\gamma - 1)M_a^2(u''_{rms}/\tilde{u})} \approx \frac{1}{Pr_t(1 - (\partial \tilde{T}_t/\partial \tilde{T}))}. \quad (4.4)$$

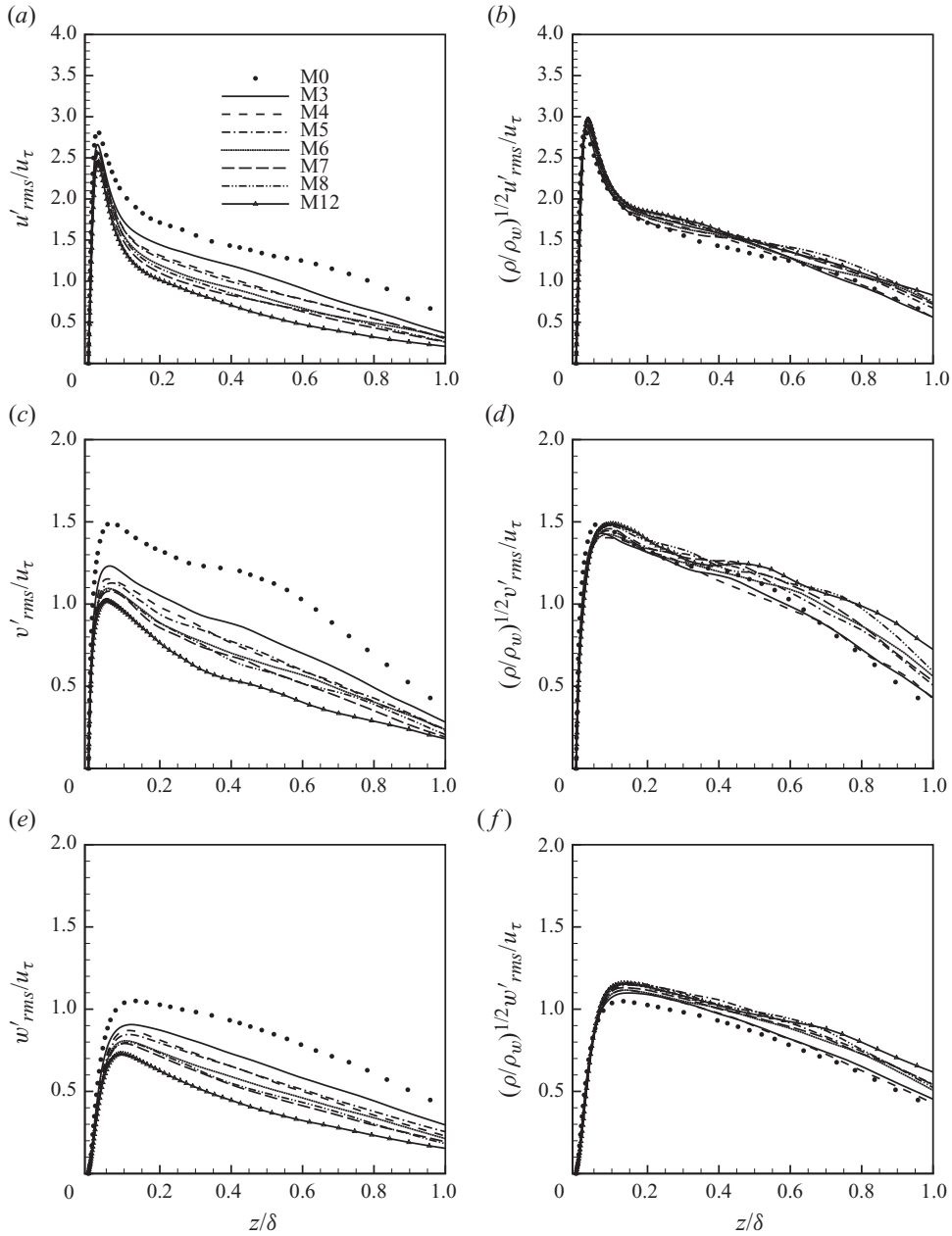


FIGURE 6. Turbulence intensities and density-weighted turbulence intensities of the (a,b) streamwise, (c,d) spanwise and (e,f) wall-normal fluctuating velocity components for different free-stream Mach number cases.

The improved performance of Huang's version of the modified Reynolds analogy is also demonstrated by the simulations of Guarini *et al.* (2000) and Maeder *et al.* (2001).

Figure 11 plots the correlation between temperature and velocity fluctuations across the boundary layer for different Mach number cases. It is shown that $-R_{u''T''}$ is not a strong function of free-stream Mach number. Through most of the boundary layer,

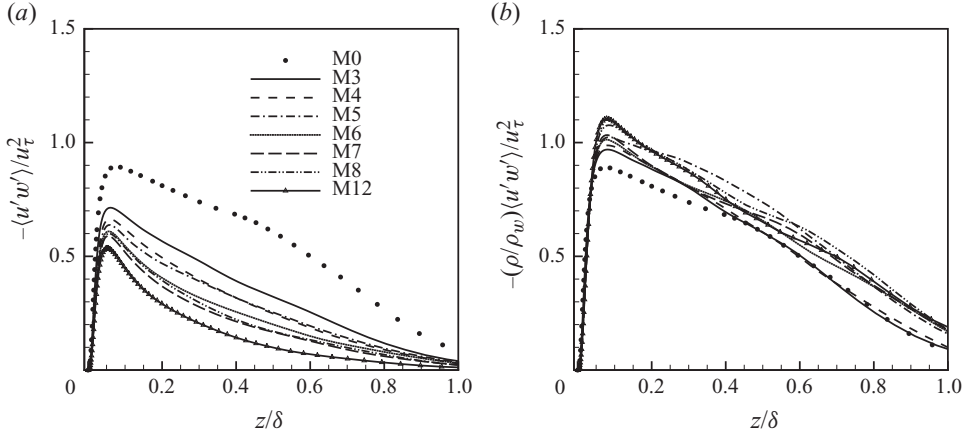


FIGURE 7. Plot of $-\overline{u'w'}$ versus z/δ , scaled by (a) $1/u_\tau^2$ and (b) $(\bar{\rho}/\bar{\rho}_w)/u_\tau^2$.

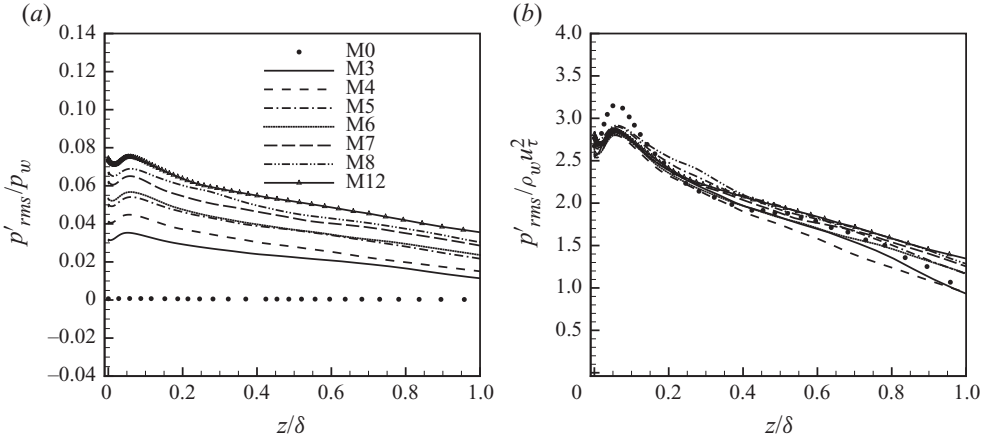


FIGURE 8. Plot of p'_{rms} versus z/δ , scaled by (a) $1/\bar{p}_w$ and (b) $1/\bar{\rho}_w u_\tau^2$.

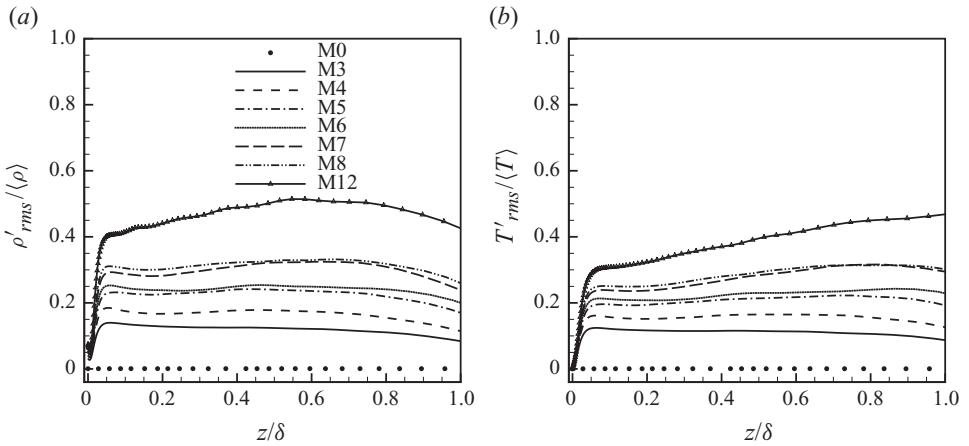


FIGURE 9. (a) $\rho'_{rms}/\bar{\rho}$ and (b) T'_{rms}/\bar{T} versus z/δ for different Mach number cases.

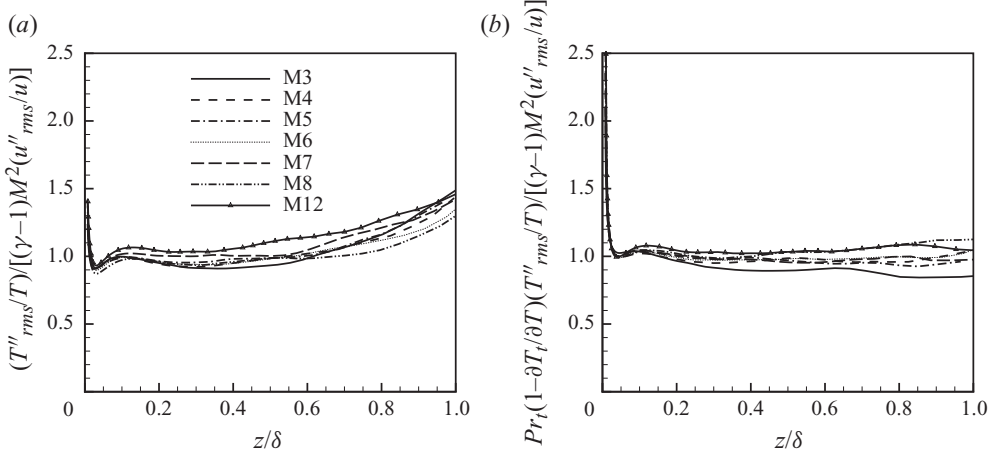


FIGURE 10. Plot of (a) the strong Reynolds analogy, as expressed by (4.1), and (b) modified Reynolds analogy by Huang *et al.* (1995), as expressed by (4.4) for supersonic Mach number cases.

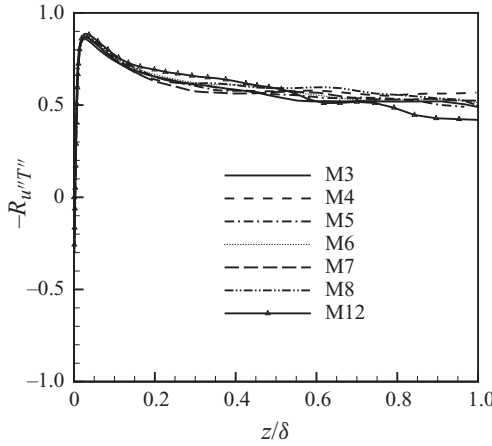


FIGURE 11. Plot of $-R_{u''T''}$ for supersonic Mach number cases.

u'' and T'' are anti-correlated and $-R_{u''T''}$ is around 0.6, similar to the results reported by Guarini *et al.* (2000).

Figure 12 plots the turbulent Prandtl number across the boundary layer. Note that Pr_t is insensitive to the free-stream Mach number condition and is close to unity in most of the boundary layer.

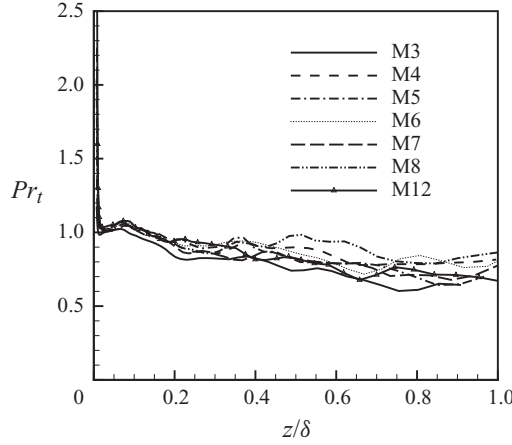
5. Turbulent kinetic energy budget

The turbulent kinetic energy is defined as

$$\tilde{k} = \frac{1}{2} \frac{\overline{\rho u_i'' u_i''}}{\bar{\rho}}, \quad (5.1)$$

and the budget equation for turbulent kinetic energy (TKE) is, after assuming homogeneity in the streamwise and spanwise directions, given by

$$\frac{\partial}{\partial t}(\bar{\rho} \tilde{k}) + \tilde{w} \frac{\partial}{\partial z}(\bar{\rho} \tilde{k}) = P + T + \Pi + \phi_{dif} + \phi_{dis} + ST, \quad (5.2)$$

FIGURE 12. Plot of Pr_t for supersonic Mach number cases.

where

$$\left. \begin{aligned} P &= -\overline{\rho u_i'' w''} \frac{\partial \tilde{u}_i}{\partial z}, \\ T &= -\frac{1}{2} \frac{\partial}{\partial z} \overline{\rho u_i'' u_i'' w''}, \\ \Pi &= \Pi_t + \Pi_d = -\frac{\partial}{\partial z} \overline{w'' p'} + \overline{p' \frac{\partial u_i''}{\partial x_i}}, \\ \phi_{dif} &= \frac{\partial}{\partial z} \overline{u_i'' \tau_{iz}'}, \\ \phi_{dis} &= -\overline{\tau_{ij}' \frac{\partial u_i''}{\partial x_j}}, \\ ST &= -\overline{w''} \frac{\partial \bar{p}}{\partial z} + \overline{u_i''} \frac{\partial \bar{\tau}_{ij}}{\partial x_j} - \bar{\rho} \tilde{k} \frac{\partial \tilde{w}}{\partial z}. \end{aligned} \right\} \quad (5.3)$$

The terms in (5.2) can be interpreted as follows. The left-hand side is the substantial derivative of the turbulent kinetic energy along a mean streamline; P is the rate of production of turbulent kinetic energy due to the mean velocity gradient; T is turbulent transport; Π includes the pressure terms (pressure diffusion and pressure dilatation, respectively); ϕ_{dif} is the viscous diffusion; ϕ_{dis} is the viscous dissipation; and ST represents terms that arise when the density is not constant. The first two terms appear due to the difference between the Favre and Reynolds averaging and the third term is the production term due to dilatation. Besides terms in ST , pressure dilatation as well as dilatational dissipation are also due to non-constant density.

Figure 13(a, b) plots the terms in the budget of turbulent kinetic energy, normalized by conventional wall variables (defined in terms of the mean density, viscosity and shear stress at the wall) and ‘semi-local’ scaling (Huang *et al.* 1995) (replacing $\bar{\rho}_w$ with $\bar{\rho}(z)$, u_τ with $u_\tau^* \equiv \sqrt{\tau_w / \bar{\rho}(z)}$ and $z_\tau^* \equiv \bar{\mu}(z) / (\bar{\rho}(z) u_\tau^*)$), respectively. The sum of all the budget terms has been included to demonstrate the overall balance and statistical convergence. It is shown that although TKE budget terms scale well in inner scaling, a better scaling is achieved when the data are scaled with local thermodynamic quantities.

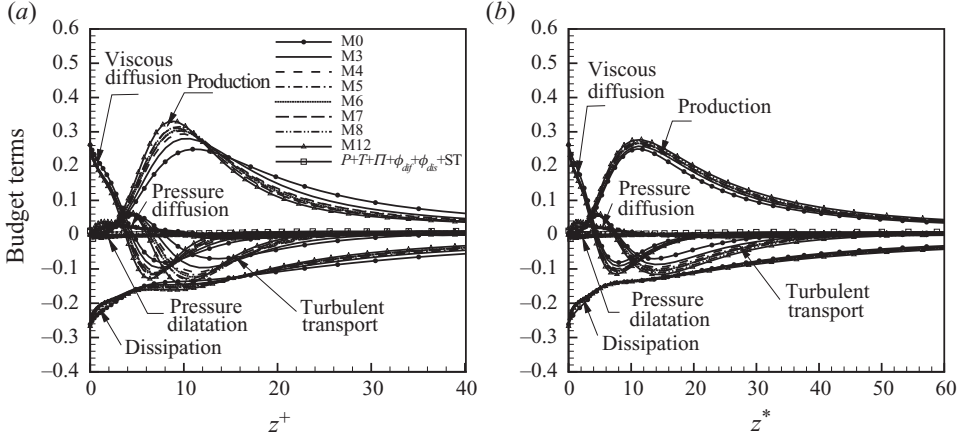


FIGURE 13. TKE budget for cases with different free-stream Mach numbers, non-dimensionalized with (a) wall units and (b) semi-local units, respectively. Variables in wall units are normalized by $\bar{\rho}_w u_\tau^2 / z_\tau$ and $z^+ = z / z_\tau$, and variables in semi-local units are normalized by $\bar{\rho} u_\tau^{*3} / z_\tau^*$ and $z^* = z / z_\tau^*$.

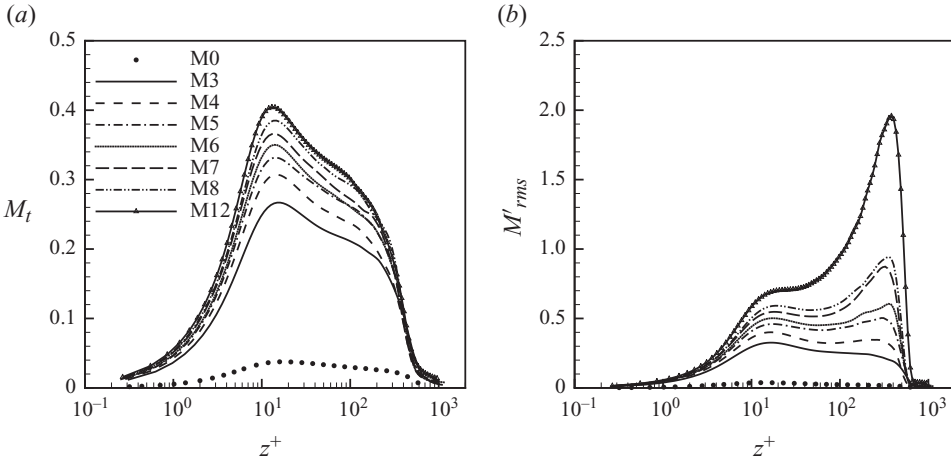


FIGURE 14. Simulation results of (a) turbulence Mach number and (b) fluctuating Mach number for various free-stream Mach number cases.

6. Compressibility effects

6.1. Turbulence Mach number

An indicator for the significance of compressibility effects is the turbulence Mach number, defined by

$$M_t = \frac{(\overline{u'_i u'_i})^{1/2}}{\bar{a}}. \quad (6.1)$$

Figure 14(a) shows that the magnitude of M_t increases significantly with increasing free-stream Mach number. The peak value of M_t increases from approximately 0.03 for M0 to 0.44 for M12. The increase in M_t indicates stronger compressibility effects with free-stream Mach number. A more significant increase is observed for the fluctuating Mach number, M'_{rms} , which is the r.m.s. fluctuation of the Mach number and thereby includes temperature fluctuations, as shown in figure 14(b). Unlike the distribution of

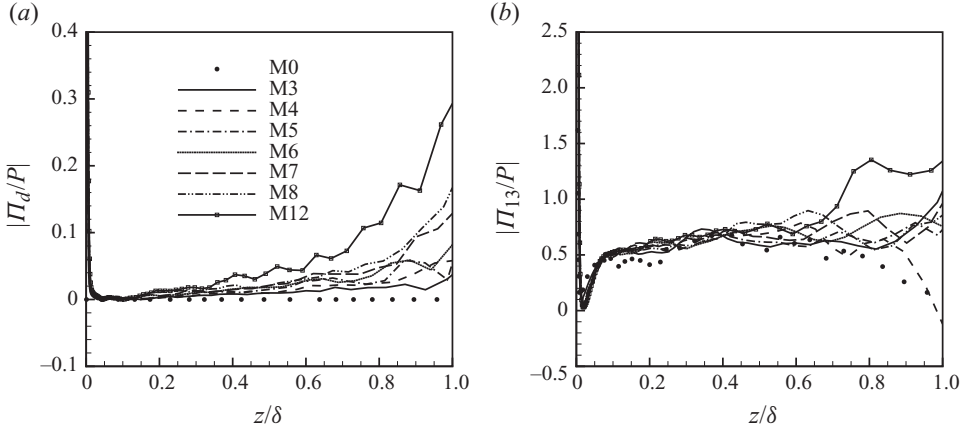


FIGURE 15. (a) Pressure dilatation Π_d and (b) pressure-strain Π_{13} for different Mach number cases normalized by production P .

M_t , the fluctuating Mach number develops a peak near the middle of the boundary layer where both the velocity and temperature fluctuations are important.

It is commonly believed that 0.3 is the threshold of M_t above which compressibility effects become important for turbulence behaviour (Smits & Dussauge 2006). The effect of compressibility can be sought by investigating explicit dilatation terms that arise from the non-vanishing velocity divergence such as pressure dilatation and dilatational dissipation. It may also be reflected in pressure-strain correlations and related to the anisotropy of the Reynolds stress tensor (Vreman, Sandham & Luo 1996).

6.2. Pressure dilatation and pressure-strain terms

One of the terms arising from the non-vanishing velocity divergence is the pressure dilatation term. Figure 15(a) plots the pressure dilatation term $\Pi_d = \overline{p'(\partial u_i''/\partial x_i)}$ for different free-stream Mach number cases. To illustrate the relative importance of Π_d compared with relevant terms in the TKE budget, Π_d is normalized by the corresponding production term $P = -\overline{\rho u_i'' w'' (\partial \tilde{u}_i/\partial z)}$ in each case. It is shown that the relative importance of Π_d increases with increasing free-stream Mach number, and the pressure dilatation term is small relative to the production term through most of the boundary layer, with a maximum ratio less than 5% for $0 < z/\delta < 0.8$. Near the boundary-layer edge, the ratio goes up to more than 10% for M8 and M12, due to the production term nearing zero.

In the study of compressible mixing layers, Vreman *et al.* (1996) found that the effect of compressibility is to change the structure of the pressure field, which results in the modification of the Reynolds stress anisotropy. Figure 15(b) plots the pressure-strain term $\Pi_{13} = \overline{p'((\partial u''/\partial z) + (\partial w''/\partial x))}$ normalized by production $P = -\overline{\rho u_i'' w'' (\partial \tilde{u}_i/\partial z)}$ for different free-stream Mach number cases. Unlike mixing layers, the pressure-strain term for boundary layers is insensitive to compressibility effects.

6.3. Dilatational dissipation

Another term arising from the non-vanishing velocity divergence is the dilatational dissipation

$$\phi_d = \frac{4}{3} \overline{\mu \frac{\partial u_i'}{\partial x_i} \frac{\partial u_k'}{\partial x_k}}. \quad (6.2)$$

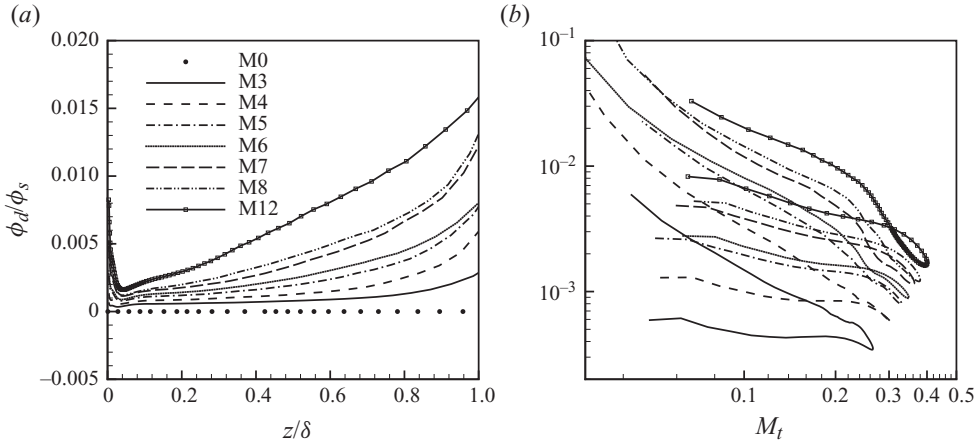


FIGURE 16. Plot of ϕ_d/ϕ_s versus (a) distance away from the wall and (b) M_t for different free-stream Mach number cases.

The solenoidal dissipation is defined as

$$\phi_s = \overline{\mu \omega'_i \omega'_i}, \quad (6.3)$$

where ω is the vorticity.

Figure 16(a) plots the ratio of ϕ_d to ϕ_s for different free-stream Mach number cases. It is shown that in most of the boundary layer, the ratio increases significantly with increasing free-stream Mach number but remains small, with a maximum value less than 5 %.

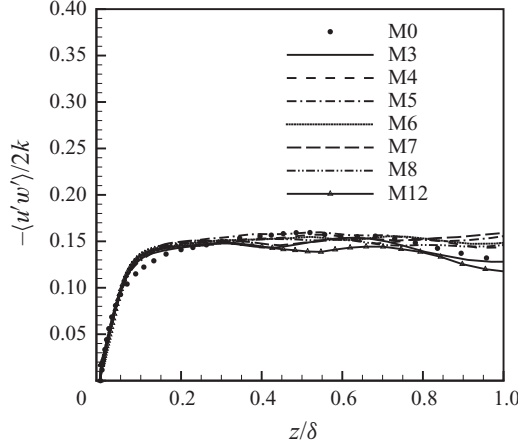
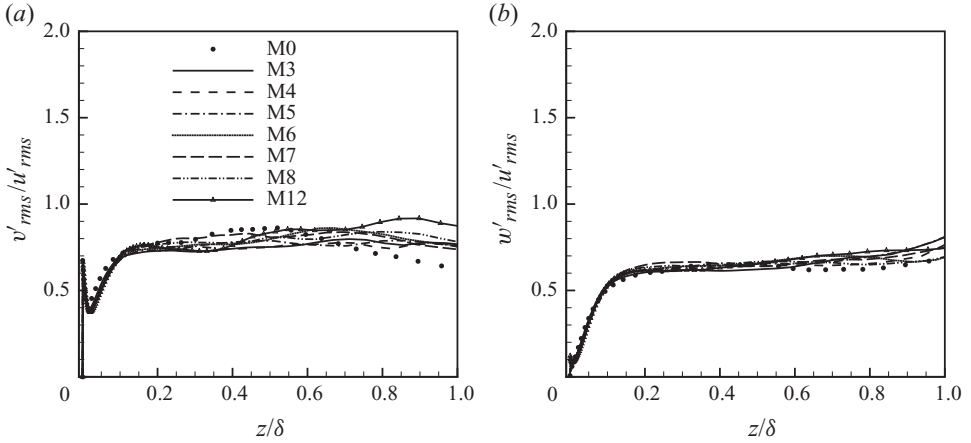
Present approaches for modelling dilatational dissipation can generally be cast into the form (Gatski 1997)

$$\phi_d/\phi_s = \alpha \mathcal{F}(M_t). \quad (6.4)$$

One of the simplest forms proposed by several authors (see Smits & Dussauge 2006) is $\mathcal{F} = M_t^4$. When the ratio ϕ_d/ϕ_s is plotted against M_t (figure 16b), it is shown that this simple form fails, similar to the results reported by Huang *et al.* (1995) and Maeder *et al.* (2001). The failure of the simple form is not unexpected, since the M_t^4 dependence of ϕ_d/ϕ_s resulted from analyses of flows with constant mean density and temperature, and the presence of mean density or temperature gradients in boundary layers can impose other dependencies. In particular, figure 16(a) shows that the overall level of ϕ_d/ϕ_s apparently depends on the mean Mach number M . The dependence of ϕ_d/ϕ_s on both M_t and M is consistent with the simple order-of-magnitude analyses of Smits & Dussauge (2006), who predicted that the fluctuating divergence, $\partial u'_i/\partial x_i$, would have a mean Mach number dependence in addition to M_t for flow with temperature inhomogeneities, and the mean Mach number dependence is related to the link between kinetic and thermal energy.

6.4. Anisotropy effects

The ‘structure parameter’ is defined as $a_1 = -\overline{u'w'}/2\bar{k}$. For incompressible flow, a_1 has been found to be approximately constant with values between 0.14 and 0.17 (Smits & Dussauge 2006). Figure 17 plots the ‘structure parameter’ for various Mach number cases. It is shown that a_1 is approximately constant for $0.1 < z/\delta < 0.9$, where it assumes values 0.14–0.16 for all the Mach number cases.

FIGURE 17. Structure parameter $-\overline{u'w'}/2k$ for various Mach number cases.FIGURE 18. Simulation results of (a) v'_{rms}/u'_{rms} and (b) w'_{rms}/u'_{rms} for different free-stream Mach number cases.

A similar trend is observed for anisotropy ratios v'_{rms}/u'_{rms} and w'_{rms}/u'_{rms} , as shown in figure 18(a,b), and both ratios assume values within the range of incompressible flows (Smits & Dussauge 2006). The near-independence of the structure parameter and anisotropy ratios on free-stream Mach numbers indicates that the change in anisotropy due to compressibility is weak, at least for the present Mach number range.

7. Structural analysis

7.1. Near-wall streaks

In this section, we investigate the effects of free-stream Mach number on near-wall streaks. Figure 19(a–c) plots the instantaneous streamwise mass flux fluctuations at $z^+ = 5$ for M0, M3 and M12. The occurrences of very long regions of negative ρu fluctuation are identified as streaks and are visible in the plots as elongated dark regions. It is shown that streaks occur in all Mach number cases, and the superficial similarity between the low-, moderate- and high-Mach-number cases is striking.

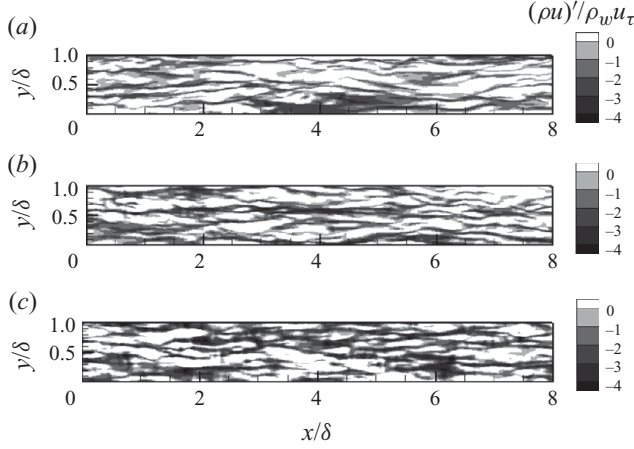


FIGURE 19. Instantaneous flow field at $z^+ = 5$ to visualize near-wall streaks for (a) M0, (b) M3 and (c) M12. Shading shows ρu fluctuations.

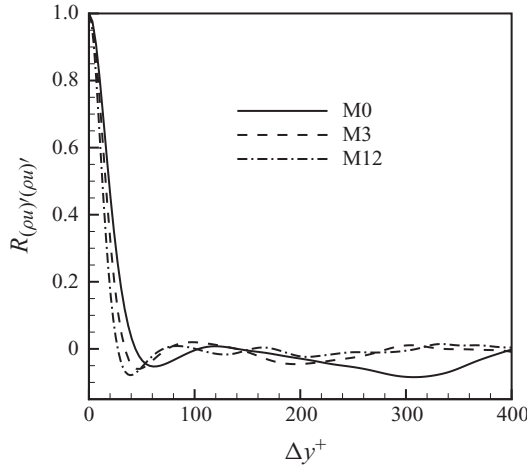


FIGURE 20. Two-point correlation $R_{(\rho u)'(\rho u)'}$ versus Δy^+ at $z^+ = 5$ for M0, M3 and M12.

As far as the spanwise spacing of near-wall streaks is concerned, figure 20 shows that an increasing free-stream Mach number slightly decreases the streak spacing, and the spanwise spacing is approximately 100 viscous wall units, similar to the values reported by Runstadler, Kline & Reynolds (1963), Kline *et al.* (1967) and Bakewell & Lumley (1967) in the study of low-speed turbulent boundary layers.

7.2. Large-scale motion

To demonstrate the large-scale turbulent bulges or large-scale motions (LSM), which are responsible for the large-scale transport of turbulence in the outer layer, figures 21(a) and 21(b) show a ‘numerical Schlieren’ visualization of a typical (x, z) plane in the boundary layer for the Mach 3 and Mach 12 cases. The contours show the magnitude of the in-plane gradient of density, $|\nabla \rho|$, scaled using an exponential function NS that highlights the full range of values, $NS = 0.8 \exp(-10|\nabla \rho|/|\nabla \rho|_{ref})$. It is shown that there are more regions of strong density gradient for M12 than M3,

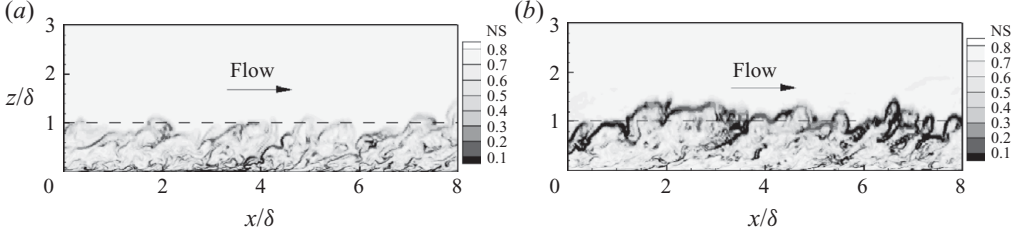


FIGURE 21. (a, b) Numerical Schlieren visualization in a (x, z) plane for Mach 3 and Mach 12.

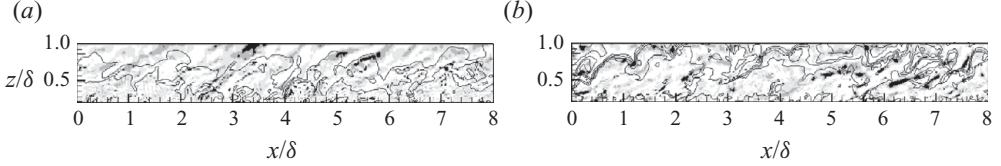


FIGURE 22. Density contour lines in a (x, z) plane for (a) Mach 3 and (b) Mach 12. The six equally spaced contours are plotted in the range $\rho/\rho_\delta \in [0.1, 1.1]$. The dark grey and black background shows regions where $-\theta > 1.5\theta'_{rms}$.

which might indicate significantly stronger compressibility and a larger number of eddy shocklets for M12.

Further evidence of the existence of eddy shocklets in boundary layers is shown by figure 22, in which the superposed contour lines of density and a grey-scale rendition of divergence field, $\theta \equiv \partial u_k / \partial x_k$, for M3 and M12 are plotted. The black areas in the figure are thin regions of very high negative divergence, which clearly show the existence of shocks. The more frequent appearance of shocklets for M12 is consistent with its relatively larger value of M'_{rms} , as shown in figure 14(b). Since for all cases shocklets have relatively small extent compared with the domain size, they are expected to have only a minor influence on most turbulence statistics, as shown in §3.

In addition, the visualizations seem to show that the LSMs cause deeper incursions of the external, irrotational flow for Mach 3 than those found for Mach 12, indicating a decrease in the wall-ward extent of entrainment or intermittency as Mach number increases. This trend is further demonstrated by intermittency function and flatness factor, as shown in figure 23, for a number of different free-stream Mach numbers. The intermittency function γ is defined as the fraction of time the flow is turbulent. In the figure, the threshold value of $(\bar{\rho u} - 3(\rho u)'_{rms})_\infty$ has been used to distinguish free-stream irrotational flow from boundary-layer flow. Both the flatness factor and the intermittency function display an apparent Mach number dependence, where the onset of intermittency (corresponding to the decrease in intermittency function or the rise in flatness factor) occurs nearer the boundary-layer edge as the Mach number increases. The hot-wire measurements of Mach 0.3 and 7 boundary layers by Klebanoff (1955), Robinson (1986), Alving (1988), Spina & Smits (1987), Smits *et al.* (1989) and Horstman & Owen (1972) have shown similar Mach number dependence. The decrease in intermittency with increasing Mach may be attributed to the decrease in the cone of influence of a flow disturbance as Mach number increases, and the turbulent–non-turbulent interface at the boundary-layer interface is confined to a small region as the Mach number increases.

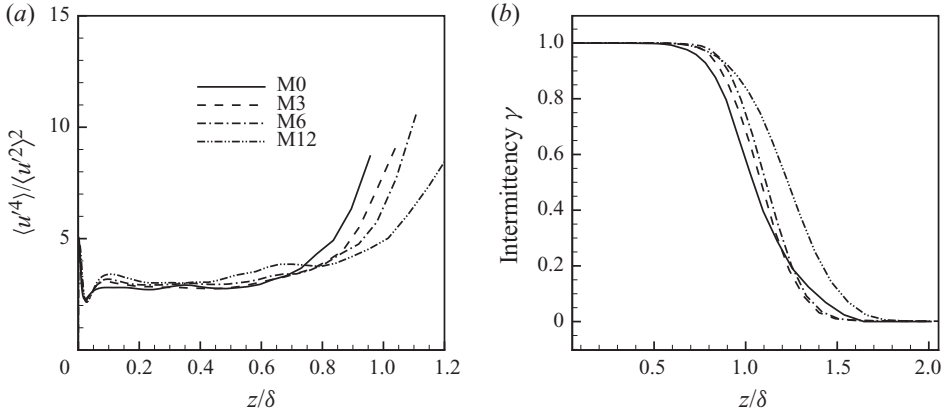


FIGURE 23. (a) Flatness factor and (b) intermittency function versus distance from the wall for different free-stream Mach number cases.

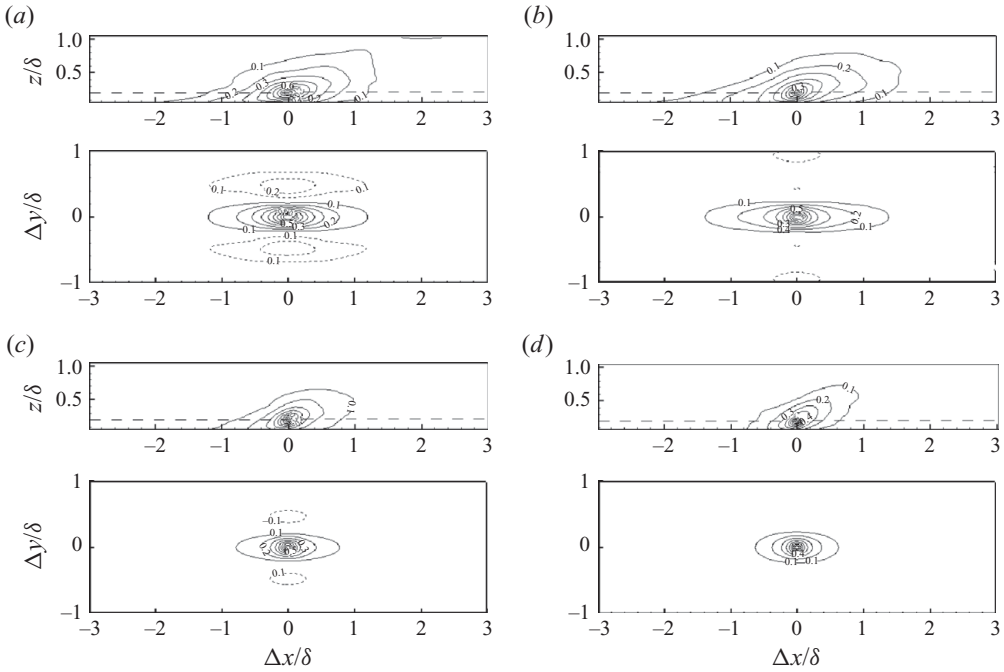


FIGURE 24. (a–d) Isocorrelation contour maps of $R_{\rho u \gamma(\rho u \gamma)}$ for M0, M3, M6 and M12, respectively. The contour maps in the streamwise–spanwise plane are plotted at $z/\delta = 0.2$.

To investigate the Mach number dependence of the size and inclination angle of the typical eddies, figure 24 plots the isocorrelation contour maps in both $(x-y)$ and $(x-z)$ planes for multiple Mach number cases. The isocorrelation contour maps are obtained by fixing ‘origin’ points at $z/\delta = 0.2$, within the logarithmic layer, and correlating them with neighbouring points lying within either a $4\delta \times 2\delta$ streamwise–spanwise window or a streamwise–wall-normal window spanning 4δ in the streamwise direction and from the upper buffer layer to the boundary-layer edge in the wall-normal direction.

The results are then averaged over all the ‘origin’ points at $z/\delta = 0.2$ and over all the flow fields.

While similar structure size and inclination angle are observed between M0 and M3, there exists an apparent decrease in the streamwise length and an increase in structure angle as the free-stream Mach number increases from 3 to 12. A similar study of structure parameters has also been conducted by Smits *et al.* (1989), in which the isocorrelation contours were compared for two boundary layers (Mach 0.1 and Mach 2.9) with Reynolds number differing by more than an order of magnitude, and they found that the streamwise scales for Mach 2.9 case were two to three times smaller than those in the Mach 0.1 case. Given the fact that our M0 and M3 cases have similar structure sizes and angles and have been conducted with approximately the same Reynolds numbers, the change observed in structure parameters by Smits *et al.* (1989) might be due to Reynolds number effects rather than Mach number effects. However, it is worth noting that the region of negative correlation is severely diminished for the Mach 3 case relative to the incompressible case, indicating that the M3 eddy’s influence on its surroundings is attenuated.

To demonstrate the wall signature of the coherent structures, we correlate the wall shear stress with the streamwise mass flux. The correlation coefficient is defined by

$$R_{\tau'_w(\rho u)'} = \frac{\tau'_w(x, y)(\rho u)'(x + \Delta x, y + \Delta y, \Delta z)}{\tau'_{w,rms}(\rho u)'_{rms}}, \quad (7.1)$$

and it has been used by several researchers to infer the existence of coherent structures (Brown & Thomas 1977; Ringuette *et al.* 2008; O’Farrell & Martín 2009).

Figure 25(a–f) plots the isocorrelation contour maps of $R_{\tau'_w(\rho u)'}$ for multiple Mach number cases in the streamwise–wall-normal and streamwise–spanwise planes. The contour plots in the streamwise–wall-normal plane indicate the existence of a downstream-leaning structure for all Mach number cases, similar to the isocontour maps of $R_{(\rho u)'(\rho u)'}$. Because this measure uses the wall shear stress, it is also an indication of the dynamic strength and organization of the structure. Isosurfaces of significant, positive $R_{\tau'_w(\rho u)'}$ can be thought of as surfaces encapsulating the low-momentum fluid in a hairpin packet corresponding to the model of Adrian *et al.* (2000). Between the legs of a hairpin vortex, the ejection of fluid causes negative $(\rho u)'$ and negative τ'_w , thus positive $R_{\tau_w(\rho u)}$. Outside the legs, the sweep events cause positive $(\rho u)'$, which correlates with the negative τ'_w between the legs to give negative $R_{\tau_w(\rho u)}$. Travelling together, multiple vortices form the packet; these coherent vortices act in concert to, on average, create and surround a region of low-momentum fluid. Both the relative size and strength are reflected in isocontours of $R_{\tau_w(\rho u)}$. The weaker positive and negative values of the correlation coefficient for higher Mach number cases indicate less organization and weaker wall signatures of hairpin packets as free-stream Mach number increases, which is consistent with the decrease in C_f with increasing Mach number, as shown in table 3. In addition, the appearance of a bump in the contour just upstream of $\Delta x/\delta = 0$ for the supersonic cases is possible evidence of a change in inter- or intra-packet organization in the streamwise direction.

8. Conclusion

We have performed DNS of turbulent boundary layers with free-stream Mach number from 3 to 12 to study the effects of Mach number on boundary-layer flow. All the Mach number cases have similar Reynolds numbers with $Re_{\delta_2} \approx 1500$. We showed that many of the scaling relations used to express compressible boundary-layer

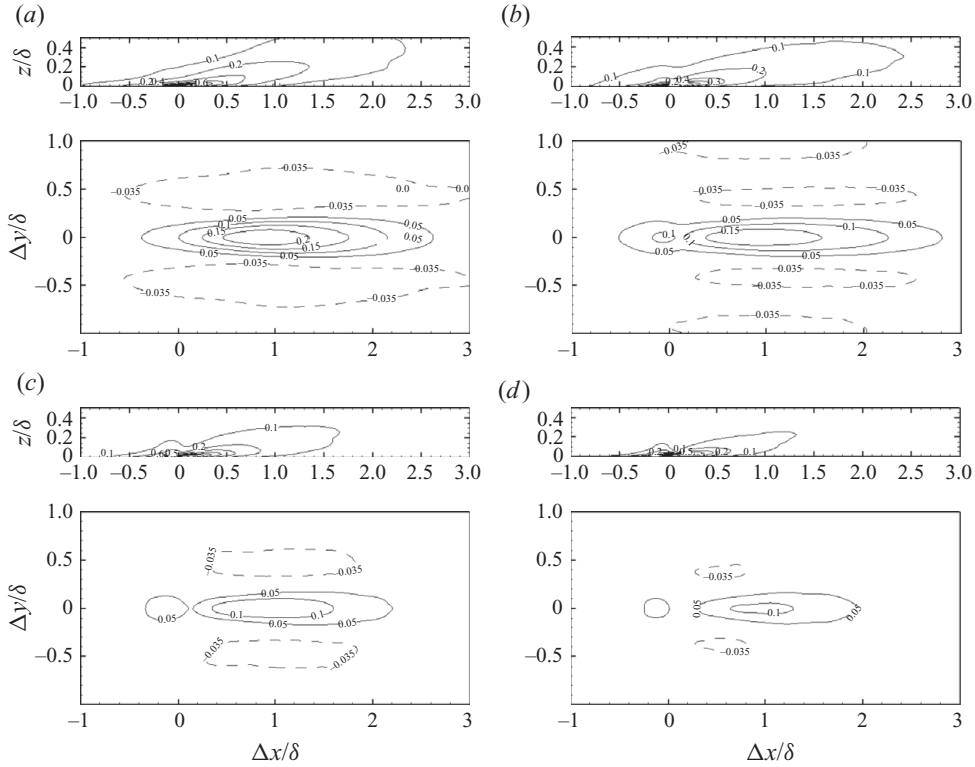


FIGURE 25. (a–d) Isocorrelation contour maps of $R_{\tau_w(\rho u)'}$ for cases M0, M3, M6 and M12, respectively. The contour maps in the streamwise–spanwise plane are plotted at $z/\delta = 0.2$ with negative contours drawn as dashed curves.

statistics in terms of incompressible boundary layers also hold for the Mach number range considered. In particular, we have shown that the van Driest transformed velocity collapses different free-stream Mach results with incompressible results. It is also shown that the r.m.s. velocity fluctuations of different Mach numbers collapse using the mean density scaling suggested by Morkovin. The mean static temperature field exhibits a quadratic dependency upon the mean velocity, as predicted by Walz's equation (3.2), for all the Mach number cases, for nearly adiabatic walls.

For the strong Reynolds analogy, we find that u'' and T'' are not perfectly anti-correlated (as predicted by the SRA, (4.2)), and $R_{u''T''}$ remains approximately the same between the different Mach number cases. The left-hand side of (4.1) weakly depends on free-stream Mach number, and a better collapse across various free-stream Mach number data is achieved using the modified version of SRA by Huang *et al.* (1995). Also, the turbulent Prandtl number is nearly constant for most of the boundary layer and insensitive to the free-stream Mach number.

In terms of the TKE budget, we show that the conventional inner scaling does not perfectly collapse the data. However, the semi-local scaling that takes into account local variation of fluid properties better collapses the data.

We find that explicit dilatation terms such as pressure dilatation and dilatational dissipation remain small for the present Mach number range, and the pressure–strain correlation and the anisotropy of the Reynolds stress tensor are insensitive to the free-stream Mach number. However, the effect of intrinsic compressibility is reflected

in several respects. The fluctuations of thermodynamic quantities (p'_{rms}/p_w , $\rho'_{rms}/\bar{\rho}$, T'_{rms}/\bar{T}) as well as the turbulence Mach numbers (M'_t , M'_{rms}) are increased dramatically when the free-stream Mach number is increased, and, correspondingly, shocklets exist and appear more frequently. The turbulence structure is also affected. Increasing free-stream Mach number results in decreased spanwise spacing of near-wall streaks, decreased streamwise extent of large-scale structures, increased structure angle and waned wall shear stress signature. Additionally, we find that with increasing Mach number, the onset of intermittency occurs nearer to the boundary-layer edge and there is less entrainment of the irrotational free-stream flow into the boundary layer.

Given the relatively low Reynolds number for current simulations, further study may be necessary to extend the results to high-Reynolds-number flows.

We thank A. J. Smits and D. Sahoo for providing PIV experimental data. This work is supported by NASA under grant NNX08ADO4A.

REFERENCES

- ADRIAN, R., MEINHART, C. & TOMKINS, C. 2000 Vortex organization in the outer region of the turbulent boundary layer. *J. Fluid Mech.* **422**, 1–54.
- ALVING, A. E. 1988 Boundary layer relaxation from convex curvature. PhD thesis, Princeton University, Princeton.
- BAKEWELL, H. P. JR & LUMLEY, J. L. 1967 Viscous sublayer and adjacent wall region in turbulent pipe flow. *Phys. Fluids* **10** (9), 1880–1889.
- BAUMGARTNER, M. L. 1997 Turbulence structure in a hypersonic boundary layer. PhD thesis, Princeton University, Princeton.
- BROWN, G. L. & THOMAS, A. S. W. 1977 Large structure in a turbulent boundary layer. *Phys. Fluids* **20** (10), S243–S252.
- DEBIÈVE, J. 1983 Etude d'une interaction turbulence/onde de choc. Phd thesis, Université d'Aix–Marseille II. In *Proc. ICHMT/IUTAM Symp. on the Structure of Turbulence and Heat and Mass Transfer*, Dubrovnik.
- DEBIÈVE, J., GOUIN, H. & GAVIGLIO, J. 1981 Momentum and temperature fluxes in a shock wave–turbulence interaction. In *Proc. ICHMT/IUTAM Symp. on the Structure of Turbulence and Heat and Mass Transfer*, Dubrovnik.
- VAN DRIEST, E. R. 1956 The problem of aerodynamic heating. *Aeronaut. Engng Rev.* **15** (10), 26–41.
- FERNHOLZ, H. H. & FINLEY, P. J. 1980 Critical commentary on mean flow data for two-dimensional compressible turbulent boundary layers. *AGARDograph* 253.
- FERNHOLZ, H. H., FINLEY, P. J., DUSSAUGE, P. & SMITS, A. J. 1989 A survey of measurements and measuring techniques in rapidly distorted compressible turbulent boundary layers. *AGARDograph* 315.
- GANAPATHISUBRAMANI, B., CLEMENS, N. & DOLLING, D. 2006 Large-scale motions in a supersonic turbulent boundary layers. *J. Fluid Mech.* **556**, 1–11.
- GATSKI, T. B. 1997 *New Tools in Turbulence Modelling*. Springer.
- GUARINI, S. E., MOSER, R. D., SHARIFF, K. & WRAY, A. 2000 Direct numerical simulation of a supersonic turbulent boundary layer at Mach 2.5. *J. Fluid Mech.* **414**, 1–33.
- HORSTMAN, C. C. & OWEN, F. K. 1972 Turbulent properties of a compressible boundary layer. *AIAA J.* **10**, 1418–1424.
- HUANG, P. G., COLEMAN, G. N. & BRADSHAW, P. 1995 Compressible turbulent channel flows: DNS results and modelling. *J. Fluid Mech.* **305**, 185–218.
- HUTCHINS, N. & MARUSIC, I. 2007 Evidence of very long meandering features in the logarithmic region of turbulent boundary layers. *J. Fluid Mech.* **579**, 1–28.
- KIM, K. C. & ADRIAN, R. J. 1999 Very large-scale motion in the outer layer. *Phys. Fluids* **11** (2), 417–422.
- KLEBANOFF, P. S. 1955 Characteristics of turbulence in a boundary layer with zero pressure gradient. *NACA Tech. Rep.* 1247.

- KLINE, S. J., REYNOLDS, W. C., SCHRAUB, F. A. & RUNSTALLER, W. P. 1967 The structure of turbulent boundary layers. *J. Fluid Mech.* **30**, 741–773.
- MAEDER, T., ADAMS, N. A. & KLEISER, L. 2001 Direct simulation of turbulent supersonic boundary layers by an extended temporal approach. *J. Fluid Mech.* **429**, 187–216.
- MARTÍN, M. P. 2004 DNS of hypersonic turbulent boundary layers. *AIAA Paper* 2004-2337.
- MARTÍN, M. P. 2007 Direct numerical simulation of hypersonic turbulent boundary layers. Part 1. Initialization and comparison with experiments. *J. Fluid Mech.* **570**, 347–364.
- MCGINLEY, C. B., SPINA, E. F. & SHEPLAK, M. 1994 Turbulence measurements in a Mach 11 helium turbulent boundary layer. *AIAA Paper* 94-2364.
- MIKULLA, V. & HORSTMAN, C. C. 1976 Turbulence measurements in hypersonic shock-wave boundary-layer interaction flows. *AIAA J.* **14** (5), 568–575.
- MORKOVIN, M. V. 1962 Effects of compressibility on turbulent flows. In *Mécanique de la Turbulence* (ed. A. J. Favre), pp. 367–380. CNRS.
- O'FARRELL, C. & MARTÍN, M. P. 2009 Chasing eddies and their wall signature in DNS data of turbulent boundary layers. *J. Turbulence* **10** (15), 1–22.
- OWEN, F. K. & HORSTMAN, C. C. 1972a Turbulent properties of a compressible boundary layer. *AIAA J.* **10** (1), 1418–1424.
- OWEN, F. K. & HORSTMAN, C. C. 1972b On the structure of hypersonic turbulent boundary layers. *J. Fluid Mech.* **53**, 611–636.
- OWEN, F. K., HORSTMAN, C. C. & KUSSOY, M. I. 1975 Mean and fluctuating flow measurements on a fully-developed non-adiabatic hypersonic boundary layer. *J. Fluid Mech.* **70**, 393–413.
- PIROZZOLI, S., GRASSO, F. & GATSKI, T. B. 2004 Direct numerical simulation and analysis of a spatially evolving supersonic turbulent boundary layer at $M = 2.25$. *Phys. Fluids* **16** (3), 530–545.
- RINGUETTE, M. J., WU, M. & MARTÍN, M. P. 2008 Coherent structures in direct numerical simulation of turbulent boundary layers at Mach 3. *J. Fluid Mech.* **594**, 59–69.
- ROBINSON, S. K. 1986 Space–time correlation measurements in a compressible boundary layer. *AIAA Paper* 86-1130.
- ROBINSON, S. K. 1991 Coherent motions in the turbulent boundary layer. *Annu. Rev. Fluid Mech.* **23**, 601–639.
- RUNSTADLER, P. S., KLINE, S. J. & REYNOLDS, W. C. 1963 An experimental investigation of flow structure of the turbulent boundary layer. *Tech. Rep.* MD-8. Mechanical Engineering Department, Stanford University.
- SAHOO, D., SCHULTZE, M. & SMITS, A. J. 2009 Effects of roughness on a turbulent boundary layer in hypersonic flow. *AIAA Paper* 2009-3678.
- SMITS, A. J. & DUSSAUGE, J. P. 2006 *Turbulent Shear Layers in Supersonic Flow*, 2nd edn. American Institute of Physics.
- SMITS, A. J., SPINA, E. F., ALVING, A. E., SMITH, R. W., FERNANDO, E. M. & DONOVAN, J. F. 1989 A comparison of the turbulence structure of subsonic and supersonic boundary layers. *Phys. Fluids* **1** (11), 1865–1875.
- SPINA, E. F. & SMITS, A. J. 1987 Organized structures in a compressible turbulent boundary layer. *J. Fluid Mech.* **182**, 85–109.
- SPINA, E. F., SMITS, A. J. & ROBINSON, S. K. 1994 The physics of supersonic turbulent boundary layers. *Annu. Rev. Fluid Mech.* **26**, 287–319.
- VREMAN, A. W., SANDHAM, N. D. & LUO, K. H. 1996 Compressible mixing layer growth rate and turbulence characteristics. *J. Fluid Mech.* **320**, 235–258.
- WALZ, A. 1969 *Boundary Layers of Flow and Temperature*. MIT Press.
- XU, S. & MARTÍN, M. P. 2004 Assessment of inflow boundary conditions for compressible turbulent boundary layers. *Phys. Fluids* **16** (7), 2623–2639.